

# Northumbria Research Link

Citation: Ong, Huiling, Pang, Huafeng, Zhou, Jian, Tao, Ran, Agrawal, Prashant, Torun, Hamdi, Thummavichai, Kunyapat, Luo, Jingting, Tao, Kai, Wu, Qiang, Chang, Honglong and Fu, Yong Qing (2022) ZnO/glass thin film surface acoustic waves for efficient digital acoustofluidics and active surface cleaning. Materials Chemistry and Physics, 287. ISSN 0254-0584

Published by: Elsevier

URL: <https://doi.org/10.1016/j.matchemphys.2022.126290>  
<<https://doi.org/10.1016/j.matchemphys.2022.126290>>

This version was downloaded from Northumbria Research Link:  
<https://nrl.northumbria.ac.uk/id/eprint/49139/>

Northumbria University has developed Northumbria Research Link (NRL) to enable users to access the University's research output. Copyright © and moral rights for items on NRL are retained by the individual author(s) and/or other copyright owners. Single copies of full items can be reproduced, displayed or performed, and given to third parties in any format or medium for personal research or study, educational, or not-for-profit purposes without prior permission or charge, provided the authors, title and full bibliographic details are given, as well as a hyperlink and/or URL to the original metadata page. The content must not be changed in any way. Full items must not be sold commercially in any format or medium without formal permission of the copyright holder. The full policy is available online: <http://nrl.northumbria.ac.uk/policies.html>

This document may differ from the final, published version of the research and has been made available online in accordance with publisher policies. To read and/or cite from the published version of the research, please visit the publisher's website (a subscription may be required.)

# **ZnO/glass thin film surface acoustic waves for efficient digital acoustofluidics and active surface cleaning**

Huiling Ong,<sup>1</sup> Huafeng Pang,<sup>2,1</sup> Jian Zhou,<sup>3</sup> Ran Tao,<sup>4,1</sup> Prashant Agrawal,<sup>1</sup> Hamdi Torun,<sup>1</sup> Kunyapat Thummavichai,<sup>1</sup> Jingting Luo,<sup>4,1</sup> Kai Tao,<sup>5</sup> Qiang Wu,<sup>1</sup> Honglong Chang,<sup>5</sup> Yong-Qing Fu<sup>1,\*</sup>

1. Faculty of Engineering and Environment, Northumbria University, Newcastle upon Tyne, NE1 8ST, UK

2. Department of Applied Physics, College of Science, Xi'an University of Science and Technology, Xi'an, 710054, P. R. China

3. College of Mechanical and Vehicle Engineering, Hunan University, Changsha 410082, P. R. China

4. Key Laboratory of Optoelectronic Devices and Systems of Ministry of Education and Guangdong Province, College of Physics and Optoelectronic Engineering, Shenzhen University, Shenzhen, 518060, China

5. Ministry of Education Key Laboratory of Micro and Nano Systems for Aerospace, Northwestern Polytechnical University, Xi'an 710072, PR China

\*Corresponding Authors: Prof. Richard Yongqing Fu, E-mail: [richard.fu@northumbria.ac.uk](mailto:richard.fu@northumbria.ac.uk)

**Abstract:** Transparent microfluidic devices based on ZnO thin film/glass surface acoustic waves (SAWs) were explored for active surface cleaning based on its acoustofluidic performance. Acoustic waves generated from ZnO films on glass substrate were investigated

and their acoustofluidic performance including transportation, jetting and nebulization were evaluated. Ash particles and starch solutions were used as model contaminants on the surface of the ZnO/glass SAW devices, and the mass loading of the contaminants on the device's surface was monitored using the SAW device with a high sensitivity of  $280.0 \pm 9.0$  Hz/( $\mu\text{g}/\text{mm}^2$ ). Active surface cleaning of the contaminants was demonstrated based on the transportation of water droplets, and optimized SAW powers were identified which caused strong interactions between water droplet and contaminants, thus effectively cleaning the surfaces. Studies of surface heating effects induced by SAWs showed that the cleaning efficiency was also influenced by the substrate temperature induced by SAW agitations.

**Keywords:** SAW, glass, ZnO film, sensing, acoustofluidics, active cleaning

## **1. Introduction**

Microfluidics provides a versatile platform with multiple functions of liquid mixing, separation, transportation, jetting, nebulization, and precise control and manipulation of biological cells or microparticles for drug delivery, lab-on-a-chip, food, and biomedical industries [1-3,4]. Acoustofluidics, which is mainly based on ultrasonics or acoustic waves, brings a revolutionary platform for biosensing and various microfluidics functions [5,6]. Innovative design and control of generation of surface acoustic waves (SAWs) on planar acoustic wave devices have been successfully developed as advanced lab-on-a-chip (LOC) platforms, providing both efficient bio-sampling and bio-sensing functions [7, 8].

Acoustofluidic devices based on SAWs are mostly fabricated on piezoelectric ceramics, such as  $\text{LiNbO}_3$  [8]. Recently, thin film-based SAWs have been extensively explored, which have advantages for realizing bendable/flexible LOC platforms, implementing highly integrated functions with microelectronics or other microfluidic/sensing techniques [8,9]. Among different types of thin film based SAW devices, ZnO film based devices on glass substrates have been widely explored for various sensing and optical applications [10,11]. These ZnO/glass SAW devices have advantages such as relatively low-temperature coefficient of frequency (TCF), high light transmission performance ( $>80\%$ ), and good optical transparency [10, 12-13]. As it is well-known, glass has been extensively used as a substrate for various applications in optics, biology, photovoltaics, and electronics. Therefore, glass-based SAW devices have great potentials to be integrated into these applications [9,11]. For examples, glass-based SAW devices can be used for transparent and flexible electronic devices [9].

There are previous studies using the ZnO/glass SAW devices for microfluidic applications. For example, acoustic streaming was demonstrated using transparent ZnO/glass SAW devices with Rayleigh waves at a high frequency of 154.9 MHz [12,14]. However, the acoustofluidic performance of ZnO/glass SAW devices (including pumping, jetting and nebulization) has seldom been reported. The key challenges in assessing acoustofluidic performance of ZnO/glass SAW device are that ZnO film typically have a poor adhesion to glass substrates and are prone to peel off [15]. In contrast, for most of these acoustofluidic applications, ZnO films with a thickness larger than one micron are normally required. Moreover, ZnO/glass SAW

devices often have a low electromechanical coupling coefficient and a low acoustic wave propagation speed as compared to those on silicon [15]. They also experience a significant heating effect due to glass's low thermal conductivity [15].

Despite these shortcomings, successfully engineered ZnO/glass SAW devices can be introduced for wide-range applications such as an active cleaning optical platform to alleviate the problems due to the accumulation of dirt and solid/liquid contaminants on glass lenses, telescope windows, or solar panels which can result in losses in energy and outputs [16]. A fully transparent ZnO/glass SAW device would be a good choice for simultaneously monitoring dust/contaminants formation through frequency shifts, while the cleaning functions will be triggered when it is needed. A feedback mechanism based on this SAW sensor could be easily implemented to verify if the surface is cleaned. Therefore, there is a strong need to investigate acoustofluidics performance and accretion–cleaning (dust and particles, etc.) characteristics of ZnO/glass SAW platform.

In this paper, transparent ZnO/glass SAW devices were fabricated and their acoustic characteristics were investigated. Acoustofluidic performance and efficiency of these ZnO/glass SAW devices were firstly evaluated including pumping, jetting and nebulization phenomena. The ZnO/glass SAW devices were demonstrated both as a sensor to detect the surface accretion (using dust and starch solutions as examples) and as an efficient actuator to drive liquid droplets for active cleaning. SAW-induced thermal effects have also been studied, exploring the issues with the acoustofluidic and cleaning performance.

## 2. Experimental

ZnO thin film was deposited on a 500  $\mu\text{m}$ -thick borosilicate glass wafer with a diameter of four inches using a direct current (DC) magnetron sputter (Nordiko) with a zinc (Zn) target (99.99% purity). Before the deposition, the glass substrates were cleaned using acetone and ethanol, and then rinsed with deionized (DI) water, and finally dried using nitrogen gas. The distance between the glass wafer on the substrate holder and the Zn target was  $\sim 20$  cm. The vacuum pressure of the chamber was maintained at  $\sim 0.35$  Pa. The rotational speed of the substrates was 4 rpm, and no external heating was applied to the substrate. During the deposition process, the surface of the Zn target was oxidized and sputtered by introducing flow of argon and oxygen gases with Ar/O<sub>2</sub> flow ratio of 10/15 sccm (standard cubic centimeter per minute). The plasma power was set at 400 Watts. Cross-section morphology of the ZnO film was observed using a scanning electron microscope (SEM, S-4100, Hitachi). Its crystalline structure was analyzed using an X-ray diffractometer (XRD, D5000, Siemens) with Ni-filtered Cu-K $\alpha$  radiation (40 kV, 30 mA,  $\lambda = 1.5406\text{\AA}$ ). Raman spectrum was obtained using a Raman spectrometer (Thermo Scientific DXR3, with a laser beam wavelength of 532 nm). Optical properties of the film deposited glass were characterized using a spectrophotometer (NKD-8000, Aquila). Photoluminescence (PL) spectra were recorded using a fluorescence spectrometer (LS-55, Perkin-Elmer) under a Xe lamp excitation with a wavelength of 325 nm.

Interdigital transducers (IDTs) consisting of 20 nm-thick Cr and 100 nm-thick Au layers were patterned using a standard photolithography and lift-off process. The designed IDTs had 50

pairs of fingers with wavelengths of 16, 32, 64, and 100  $\mu\text{m}$ . The reflection spectra ( $S_{11}$ ) and transmission spectra ( $S_{12}$ ) of the SAW devices were measured using a radio frequency (RF) network analyzer (Keysight, FieldFox N9913A). The impedance of the input port at the resonant frequency ( $f_0$ ) was measured using the Smith Chart function of the network analyzer. The electromechanical coupling coefficient ( $k^2$ ) was calculated using the following equation:

$$k^2 = \frac{\pi}{4N} \left( \frac{G}{B} \right)_{f=f_0}, \quad (1)$$

where  $N$  is the finger pairs of the IDTs;  $G$  and  $B$  are the radiation conductance and susceptance of the input port at the resonant frequency obtained from the Smith chart of the network analyzer, respectively [17].

Acoustofluidics tests were performed using the ZnO/glass SAW devices, and functions of transportation (or pumping), jetting and nebulization of water droplets were demonstrated. For nebulization tests, the ZnO/glass SAW devices were directly used without any surface treatments, and a 2  $\mu\text{L}$  of de-ionized (DI) water droplet was agitated with the applied SAW power. For droplet transportation and jetting studies, the surfaces of the ZnO/glass SAW devices were uniformly coated with a layer of CYTOP (Asahi Glass Co.) to create a hydrophobic layer [18]. An RF signal at the resonant frequency of the SAW device was generated using a signal generator (Aim TTi, TG5011A) and then amplified using a power amplifier (Amplifier Research, Model 75A250). The RF power applied to the IDTs of the SAW devices was measured using an RF power meter (Racal Instruments 9104).

To demonstrate dust monitoring and cleaning functions, SAW devices with wavelengths of 100

$\mu\text{m}$  and  $64\ \mu\text{m}$  were used. Surfaces of the IDTs were coated with different masses of ashes (from incense sticks), and starch solutions in their semi-solid and liquid forms, all as the models for surface contaminants. For these tests, surfaces of the SAW devices were pre-treated with a hydrophobic surface layer of CYTOP, to facilitate movement of water droplets along the surface, and various RF powers were applied on these SAW devices.

Temperature coefficient of frequency (TCF) of the SAW device is associated with its thermal stability and linked with the temperature expansion coefficients of both ZnO and glass. To obtain the TCF value, the ZnO/glass SAW devices were heated from  $20^{\circ}\text{C}$  to  $60^{\circ}\text{C}$  in an oven (Carbolite) while their resonant frequencies were monitored using the network analyzer. The TCF values were obtained based on the shifts in their resonant frequencies within a temperature range from  $20^{\circ}\text{C}$  to  $60^{\circ}\text{C}$ , using the following equation:

$$TCF = \frac{1}{f_0} \frac{df}{dT} \text{ (ppm}/^{\circ}\text{C}) \quad (2)$$

where the TCF is expressed as parts per million of frequency shift per degree Celsius ( $\text{ppm}/^{\circ}\text{C}$ ).

To evaluate surface heating effects during the acoustofluidics and cleaning processes, an infrared (IR) camera (FLIR, T620bx) was used to monitor the temperature changes on the surface of the SAW devices at different frequencies and powers. Furthermore, the changes in temperature during pumping and nebulization were also recorded using the IR camera at different SAW powers, for the ZnO/glass SAW devices with different frequencies.

### 3. Results and discussion



### 3.1. ZnO film characterization

Figure 1 shows cross-section microstructure of ZnO film on the glass substrate, indicating a vertically columnar structure. The film thickness was determined to be 4.17  $\mu\text{m}$ . Figure 1b shows the XRD pattern of the ZnO film on a glass substrate. A strong peak at  $33.90^\circ$  corresponds to the (0002) plane of ZnO film, which shows the *c*-axis preferential growth of the wurtzite ZnO film. Figure 1c shows the vibration modes of the ZnO films from the Raman spectrum of the ZnO film. The sharp peak at  $100\text{ cm}^{-1}$  is assigned to non-polar modes of  $E_2(\text{low})$  [18]. Two strong and broad peaks at  $432\text{ cm}^{-1}$  and  $575\text{ cm}^{-1}$  correspond to the  $E_2(\text{high})$  and  $A_1(\text{LO})$  vibration modes of ZnO, respectively [19, 20]. The weak peak at  $326\text{ cm}^{-1}$  is originated from the second-order mode of Raman scattering [21, 22]. Figure 1d shows the transmission spectra from the ultra-violet visible spectrophotometer of the ZnO film on the glass. The optical transmittance value is larger than 70% within the measured wavelength range of 450 to 800 nm. The defects of ZnO films on the glass substrate can be identified from the PL spectrum shown in Figure 1e. A wide band with multiple peaks of 404 nm, 423 nm, 461 nm and 485 nm is assigned to the complex defects. Those two peaks at 404 nm and 423 nm correspond to zinc vacancies, and those two peaks at 461 nm and 485 nm are related to the oxygen vacancies [19]. A weak peak at 523 nm is originated from the singly-ionized oxygen vacancies on the ZnO surface [19].

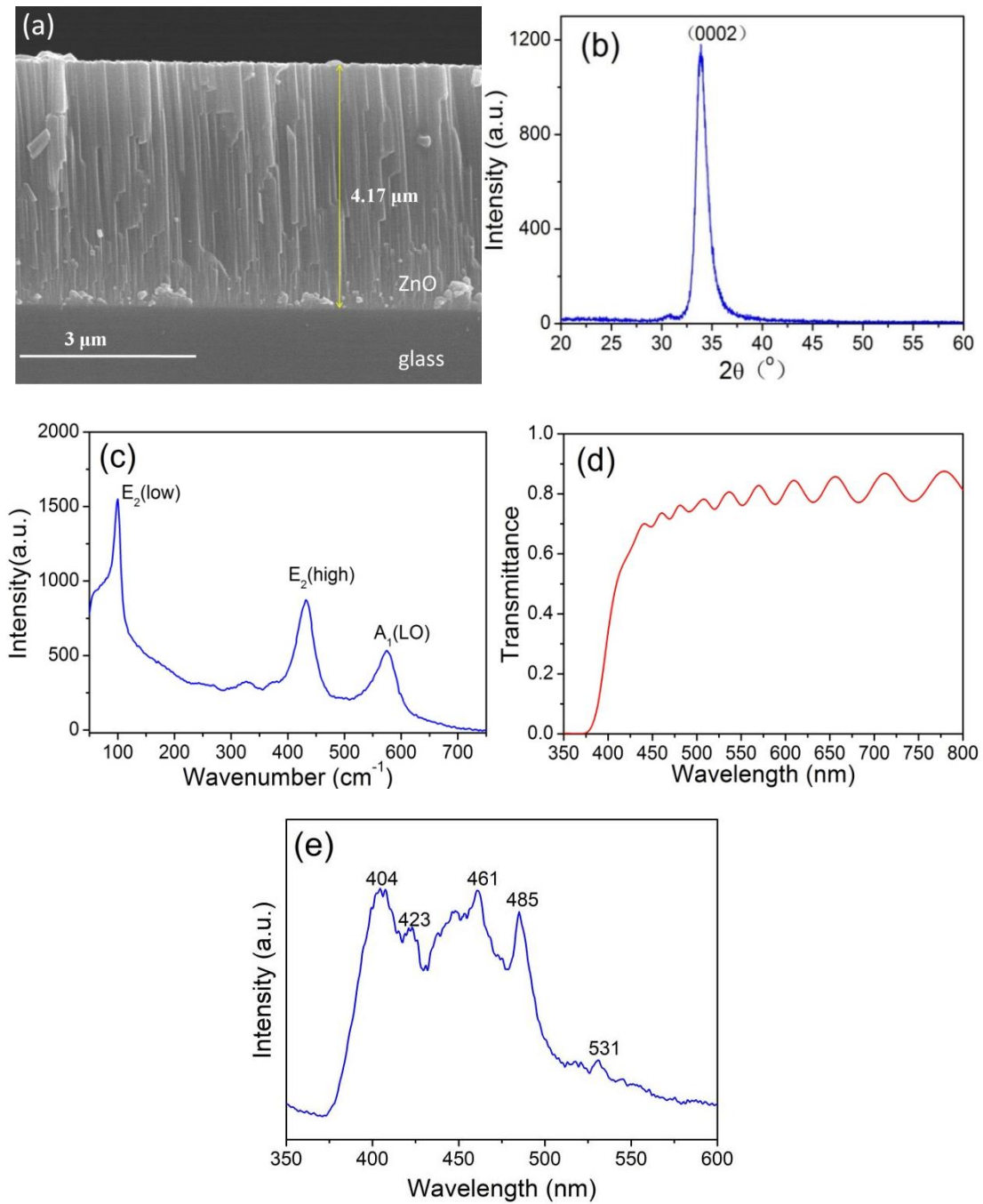


Figure 1: (a) Cross-section morphology of the ZnO film deposited on glass; (b) XRD pattern; (c) Raman spectrum of the ZnO film on glass substrate; (d) UV-VIS transmission spectra of ZnO film on glass; (e) Photoluminescence spectrum of ZnO film on glass substrate excited using a wavelength of 325 nm at room temperature

In brief, all the above film characterization results showed that the ZnO film on glass substrate

has a good crystallinity, *c*-axis orientation, and transparency, which are suitable for piezoelectric and SAW applications.

### **3.2. ZnO/glass SAW device characterization**

Numerical simulations were performed to investigate the resonant frequencies and wave modes of the ZnO/glass SAW devices. This was done using finite element analysis (FEA) with commercial software (COMSOL 5.1) based on a two-dimensional (2D) strain model of a piezo plane. For the simulations, a 5  $\mu\text{m}$ -thick ZnO film was modeled on a 120  $\mu\text{m}$ -thick glass substrate that was imposed a fixed boundary condition at the bottom. The reason to select a thinner glass in this model is to reduce simulation complexities, while the selected thickness is still large enough for penetrations of the acoustic wave into the substrate without affecting the results. A free and zero charge/symmetry boundary condition was assigned to the top surface of the piezoelectric ZnO layer. Periodical boundary conditions were adopted for both sides in this model. A polarization voltage value of 1 V was applied to one 200 nm-thick aluminum electrodes, while the second electrode was assigned to be electrical ground. The material constants were extracted from the material library of COMSOL. The wavelength of the devices was changed from 16 to 100  $\mu\text{m}$ .

Figure 2a shows examples of the obtained theoretical impedance and experimental reflection spectra ( $S_{11}$ ) of the ZnO/glass SAW device with a wavelength of 100  $\mu\text{m}$ . The resonant frequency of the Rayleigh wave was found to be 28.12 MHz from both the simulation and

experimental results. The Sezawa mode appears at 51.53MHz. The multiple peaks centered around 126.28 MHz are assigned to the higher-order (harmonic) modes. The particle vibration profiles of different wave modes are presented in Figures 2b-2d, which confirms the acoustic characteristics of the above three modes.

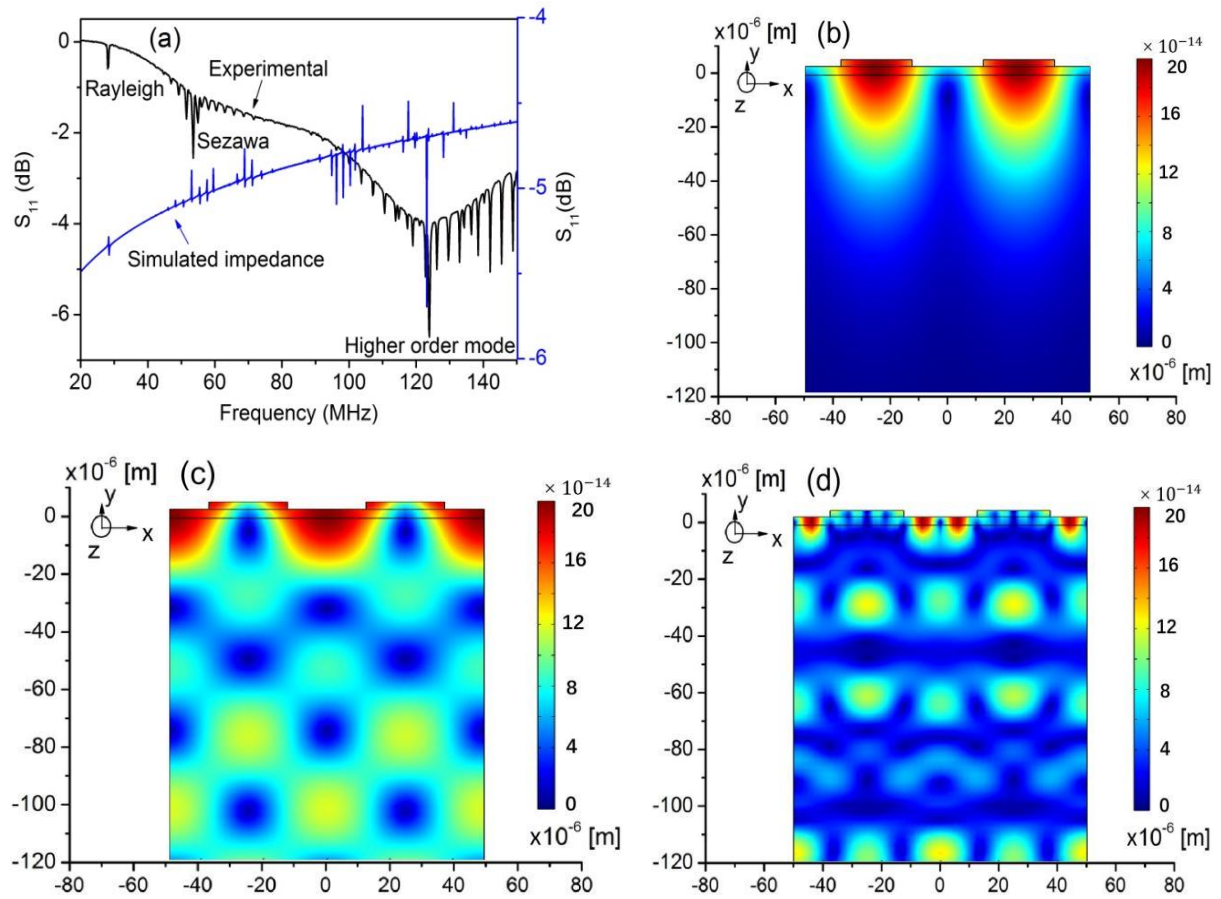
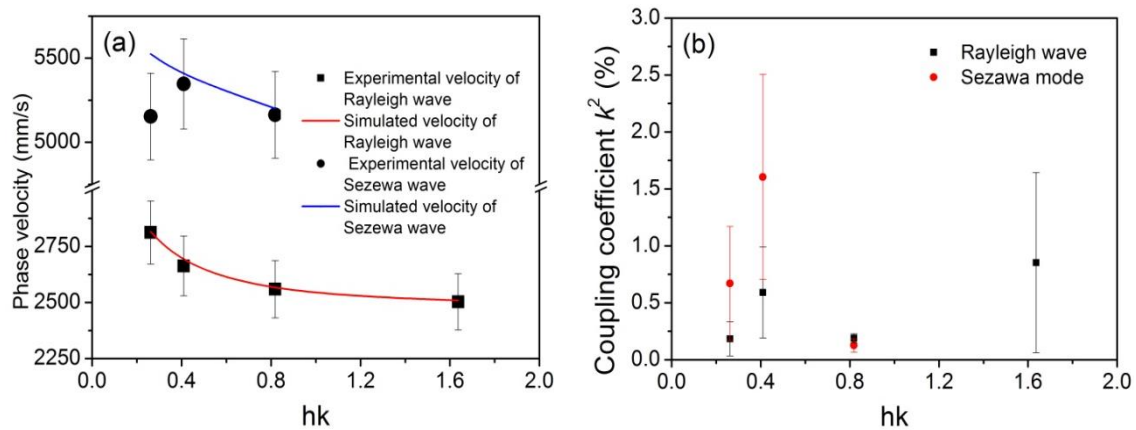


Figure 2. (a) frequency response ( $S_{11}$ ) of the ZnO/glass SAW device with a wavelength of 100  $\mu\text{m}$ ; particle vibrations of the three modes: (b) Rayleigh wave, (c) Sezawa mode and (d) higher order mode.

Figures S1(a, d and g) in the supporting information show the obtained theoretical impedance and experimental reflection spectra ( $S_{11}$ ) of the ZnO/glass SAW devices with wavelengths of

64, 32, and 16  $\mu\text{m}$ . The resonant frequencies of the Rayleigh waves are 41.60 MHz, 79.98 MHz, and 155.25 MHz based on simulation and experimental results for devices with wavelengths of 64, 32, and 16  $\mu\text{m}$ , respectively. Their Sezawa modes appear at 83.55 MHz and 161.35 MHz for devices with 64  $\mu\text{m}$  and 32  $\mu\text{m}$  wavelengths, respectively. These have been verified from the simulation results as can be seen in the simulated impedance of those devices. The particle vibration profiles of these modes are further shown in Figures S1b to S1h.

Figure 3(a) shows the phase velocities of Rayleigh and Sezawa wave modes as a function of the normalized thickness ( $hk$ ,  $h$  is 4.17  $\mu\text{m}$ ,  $k = 2\pi/\lambda$ ,  $\lambda$  is 100, 64, 32, and 16  $\mu\text{m}$ ). The phase velocity of Rayleigh wave changes from 2503 m/s to 2812 m/s with increase of the normalized thickness from 0.26 to 1.64. The velocity of Rayleigh wave propagating in ZnO (2700 m/s) is smaller than that in glass (3200 m/s) [9, 10]. The dispersion effect of the phase velocity is significantly influenced by the penetrating depth of the acoustic wave into the glass substrate when the wavelength is increased from 16  $\mu\text{m}$  to 100  $\mu\text{m}$  [9]. The phase velocity of Sezawa mode waves is increased from 5163 m/s to 5347 m/s, which shows a similar characteristic of the velocity dispersion, compared with those of the Rayleigh waves as shown in Fig. 3(a).



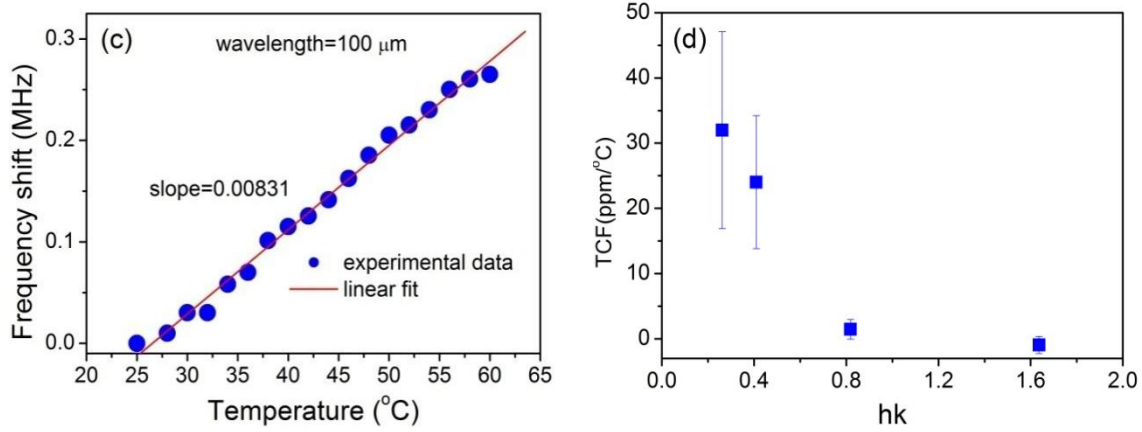


Figure 3. (a) Phase velocities and (b) Coupling coefficients of the ZnO/glass SAW devices as a function of the normalized thickness; (c) Frequency changes of the Rayleigh wave with the temperature for the ZnO/glass SAW device with a wavelength of 100 μm, and (d) the TCFs as a function of the normalized thickness.

Figure 3(b) shows the obtained average values of electromechanical coupling coefficient  $k^2$  for the Rayleigh waves of the devices with different wavelengths. The  $k^2$  values are changed from 0.18%, 0.29%, 0.19% to 0.85% with the increase of the normalized thickness, as shown in Figure 3(b). These values are much lower than those on silicon substrates (3% to 4%). Zhou et al. previously reported that the  $k^2$  values of the Rayleigh wave SAW devices were decreased from 1.8 % to 0.5% as the wavelength of the SAW devices is increased from 16 to 32 μm [12]. As the wavelength is increased, the energy is mostly dispersed into the non-piezoelectric glass, which ultimately results in a reduction in the  $k^2$  values [9, 12]. The maximum value for Sezawa mode is 1.6% at a normalized thickness of 0.41, which is slightly larger than those reported in the literature (e.g., 0.45 to 0.50 %) [23,24]. For the Sezawa mode, as its frequency is much higher, the wave energy is more confined to the interface and the ZnO thin film, which ultimately leads to a larger coupling coefficient [25-27]. It was reported that the  $k^2$  values of

Sezawa wave mode are decreased as the wavelength is increased [12].

Figure 3(c) shows the frequency shifts of Rayleigh wave for the ZnO/glass SAW device with a wavelength of 100  $\mu\text{m}$  between the temperatures of 25°C and 60°C, and the obtained TCF value has a positive value of 44.33 ppm/°C. Figure 3(d) shows the average TCF values of the SAW devices decrease with the normalized thickness. This is mainly because at smaller wavelengths, the propagation of the acoustic wave is mainly confined in the piezoelectric ZnO film [28]. Moreover, the TCF value of glass is generally positive, and the TCF value of ZnO is negative. The TCF values approach zero with the increase in the normalized thickness, which is very good for sensing applications to avoid influences of ambient temperature. It was noted that the TCF values of SAW devices that consist of common piezoelectric materials such as LiNbO<sub>3</sub>, AlN, and GaN are dramatically different [29]. To be compared with, those TCF values for the ZnO/Si, LiNbO<sub>3</sub> and ZnO/Al SAW devices are from -18 ppm/°C, to -75 ppm/°C, and then up to -600 ppm/°C [30].

### **3.3. Acoustofluidic performance**

Figures 4(a-c) show the snapshots of the droplet transportation at a power of 3.99 W using the Rayleigh mode of the SAW device with a wavelength of 100  $\mu\text{m}$  (at a resonant frequency of 28 MHz). The droplet has been transported on the substrate surface where the pumping speed of the water droplet is dependent on the size of the water droplet and surface treatment of the ZnO/glass SAW device [30]. With an increase in the power applied on the same SAW device,

the pumping speed of the water droplet increases as shown in Fig. 4d.

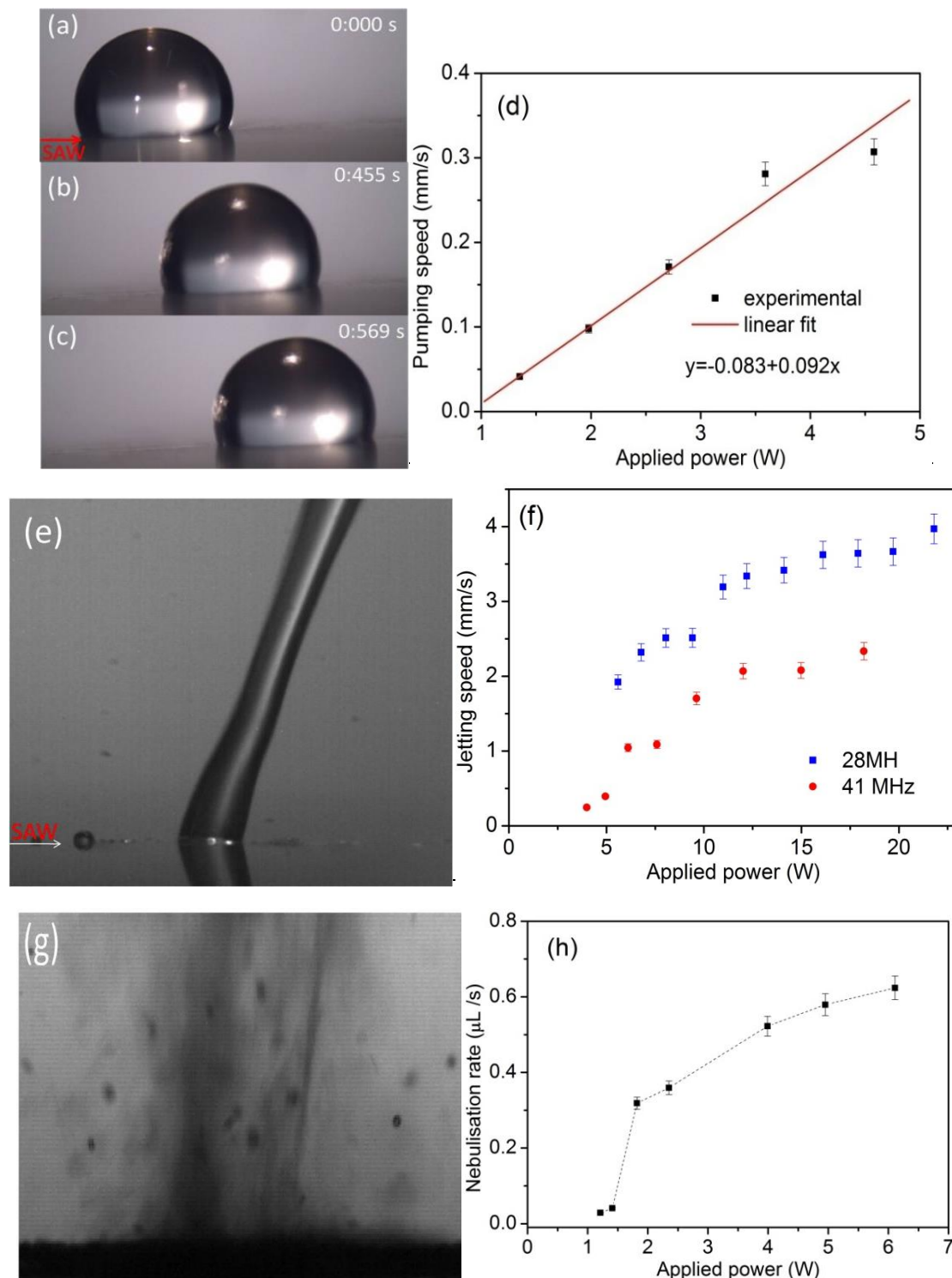


Figure 4. Droplet pumping of a water droplet of  $2\mu\text{L}$  on the surface of ZnO/glass SAW devices with a wavelength of  $100\mu\text{m}$  applied using a power of  $3.99\text{ W}$  at the time of (a) 0



s; (b) 0.455 s and (c) 0.569 s, respectively; (d) droplet pumping speed versus the applied power for ZnO/glass SAW device with a resonant frequency of 28 MHz; (e) snapshot of the droplet jetting on the surface of ZnO/glass SAW devices with a wavelength of 100  $\mu\text{m}$  applied using a power of 9.62 W; (f) droplet jetting speed versus the applied power for ZnO/glass SAW devices with resonant frequencies of 28 MHz and 41MHz; (g) nebulization behavior of 1  $\mu\text{L}$  water droplet on the surface of ZnO/glass SAW devices with a resonant frequency of 28 MHz applied using a power of 2.35 W; (b) the nebulization rate versus the applied power.

When the power applied is increased above 4 W, the water droplet was observed to eject from the surface instead of just moving or sliding on the surface of the SAW device. Figure 4e shows that with a relatively high power of 9.62 W, acoustic energy coupling into the water droplet becomes so large that the water droplet can be deformed into an elongated liquid column and ejected from the surface after 0.558 s [26]. Figure 4f shows the jetting speeds which were calculated as the distances moved by the droplet along the ejected direction in the horizontal plane, divided by the time to experience the whole jetting phenomenon. Similar trends were observed for both samples of 28 MHz and 41 MHz with the increase of RF power, whereas the jetting speed for 78 MHz seems to be decreased (all the results are shown in the supporting information). This decrease in jetting is probably because at a higher frequency, the energy is dissipated much faster into the water droplet.

The jetting angle is linked to the Rayleigh angle  $\theta_R$ , which can be calculated using the speed

of sound in water  $V_L$  (1480 m/s) and wave propagation velocities in solid  $V_s$  [31], based on the following equation [32]:

$$\theta_R = \sin^{-1} V_L / V_s \quad (3)$$

The calculated values of Rayleigh angles for the SAW devices with different wavelengths are summarized in Table S1. These calculated angles are between  $31.73^\circ$  and  $36.17^\circ$ . The measured results of the jetting angles showed that they are ranged from  $30.6^\circ \pm 1.2^\circ$  to  $34.6^\circ \pm 1.0^\circ$ , which are following those of the Rayleigh angles. The differences between the calculated and measured values of Rayleigh angles are caused by the surface treatment, applied power, and the size of the water droplet as reported in Ref. [25].

Figure 4g shows an example of high-speed images of nebulization phenomena of a water droplet (on untreated device surface) obtained using the SAW device with the wavelength of  $100 \mu\text{m}$  and a power of 2.35 W. When the power is applied to the SAW device, the pressure from the acoustic waves drives the water droplet and causes the significant vibration of the hemispherical surface, resulting in the formation of capillary waves and ejected tiny droplets [33]. When the nebulization process occurs, a mist of different sizes of the tiny droplets are ejected from the surface in various directions, as can be seen in Figure 4g. For the nebulization, the average nebulization speed is defined as the volume of the water droplet divided by the time for the water droplet to be fully nebulized. Figure 4h shows the obtained nebulization speeds as a function of the applied power. As the power is increased, the nebulization time for the  $1 \mu\text{L}$  water droplet to be fully nebulized is gradually reduced, with slight fluctuations observed. The nebulization speed is observed to increase with the SAW power applied, which

is linked with the fast nebulization process at a much larger power value [32].

In brief, the above acoustofluidics result shows that the ZnO/glass SAW device with a frequency of 28 MHz presents good acoustofluidic performance in terms of pumping, which would be useful for cleaning applications as other frequency samples would most likely result to jetting phenomenon. In terms of jetting, the results shown above could be effectively used in applications such as 3D printing [32].

### 3.5. Demonstration of dust sensing and surface cleaning

#### *Detection of dust formation based on mass-loading effect*

Figure 6a shows the frequency shifts ( $\Delta f$ ) as a function of the mass area ratio ( $m/A$ ) of dusts (using ashes as examples) for the mass loading testing on four SAW devices with different wavelengths. The frequency shift of the SAW devices gradually increases with the mass area ratio loaded on top of the IDTs. To determine the sensitivity, a linear fit between the frequency shift and mass area ratio was performed in the linear region of the variations from 475.7  $\mu\text{g}/\text{mm}^2$  to 964.3  $\mu\text{g}/\text{mm}^2$ . The sensitivity is obtained as  $5.7 \pm 2.1 \text{ Hz}/(\mu\text{g}/\text{mm}^2)$ ,  $8.6 \pm 1.8 \text{ Hz}/(\mu\text{g}/\text{mm}^2)$ ,  $15.5 \pm 5.5 \text{ Hz}/(\mu\text{g}/\text{mm}^2)$  and  $280.0 \pm 9.0 \text{ Hz}/(\mu\text{g}/\text{mm}^2)$ , which increases with the resonant frequency of SAWs excited using different wavelengths. Figure 6b shows the experimentally obtained sensitivity results, compared with those calculated using the following equation:

$$S = \frac{\Delta f}{m/A} = Kf_0^2 \quad (4)$$

where  $K$  is a piezoelectric constant that is related to the film [35]. The deviations between the experimental and theoretical results are possibly caused by the variations of the coupling interaction of the dust with ZnO film, mainly including the physical adsorption [34,35].

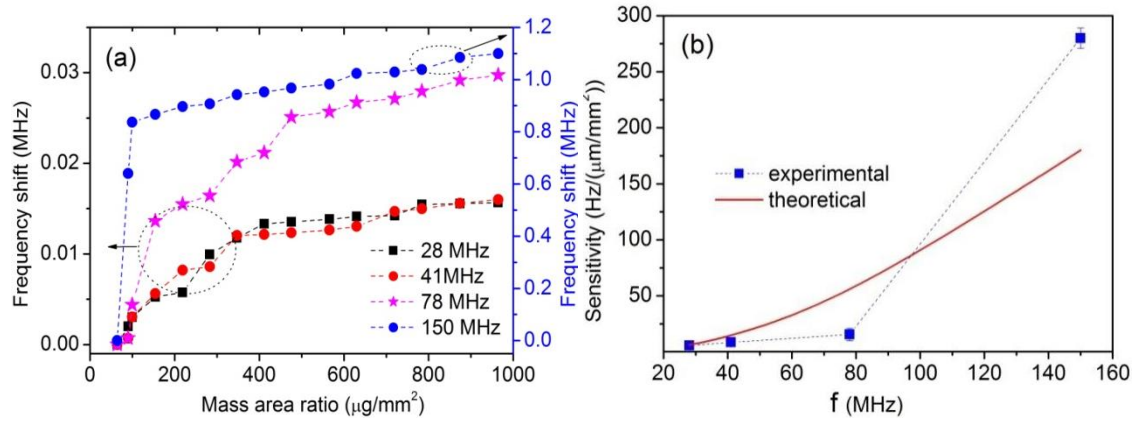
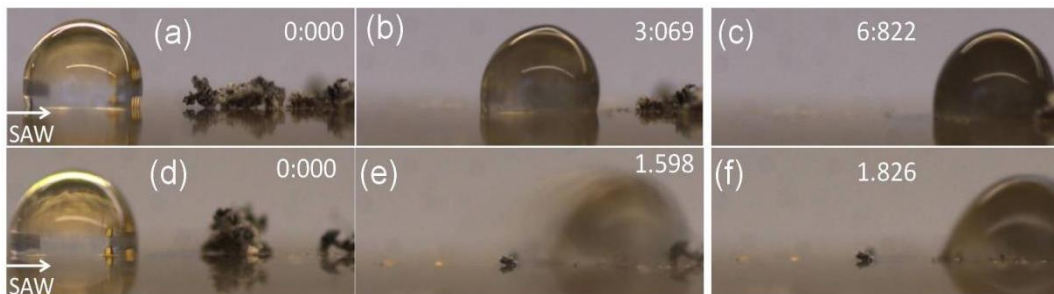


Figure 6: (a) Frequency shift vs mass per unit area of ash particles on SAW devices with wavelengths (resonant frequency) of 100  $\mu\text{m}$  (28 MHz), 64  $\mu\text{m}$  (41 MHz), 32  $\mu\text{m}$  (78 MHz), and 16  $\mu\text{m}$  (150 MHz); (b) Sensitivity versus the frequency of the ZnO/glass SAW device for mass loading testing of ash particles.

### ***Demonstration of active cleaning***



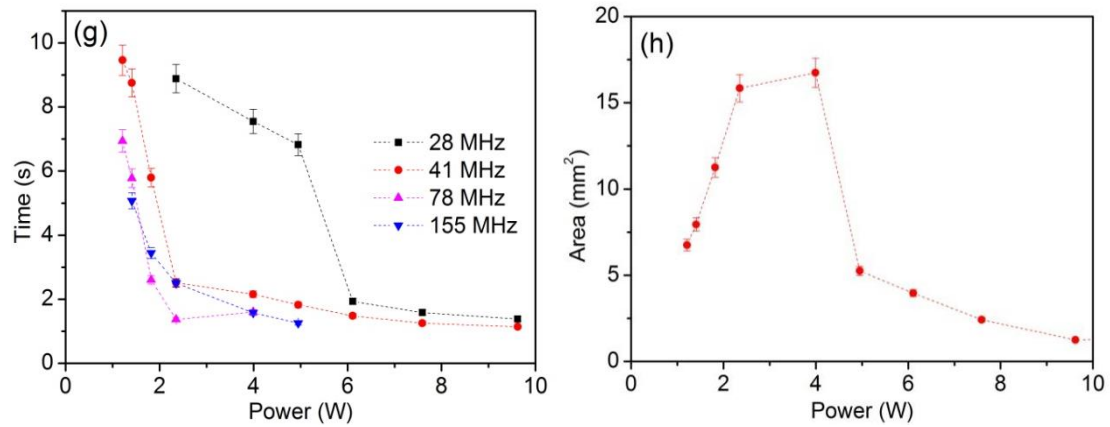


Figure 7: Droplet transportation behaviors of a 2  $\mu\text{l}$  droplet at a power of 4.95 W for 28 MHz SAW device (a) 0 s; (b) 3.069 s; (c) 6.822 s; and for 41 MHz SAW device (d) 0 s; (e) 1.598 s; (f) 1.826 s; (g) Time taken (s) for water droplet to drive away ash particles versus power applied for all four different SAW devices of different frequencies; (h) Area versus power as a measure of cleaning efficiency on 64  $\mu\text{m}$  SAW device.

Active cleaning demonstrations were conducted using the SAW devices with a frequency of 28 MHz (wavelengths of 100  $\mu\text{m}$ ), with the ashes put onto the SAW propagating paths. Figures 7a-7c show examples of the cleaning stages of ash particles on the surface of the SAW device with a wavelength of 100  $\mu\text{m}$  at an applied power of 4.95 W. When the droplet encounters the ash particles during the pumping process, the ash particles are quickly mixed into the water droplet and then driven away [36]. During the process, droplets were pumped at different speeds and moved along the propagating path of the SAWs. Figures 7d-7f show the obtained cleaning results on the 64  $\mu\text{m}$  SAW device. The water droplet was driven at an RF power of 4.95W, and the ash particles were taken away by the moving water droplet at a much higher speed as compared to the 100  $\mu\text{m}$  SAW device [36].

Figure 7g shows that for the 100  $\mu\text{m}$  (28 MHz) SAW device, the water droplet is observed to experience pumping where at a power of 4.95 W is suitable for cleaning work for driving away ash particles. When the frequency increases (where wavelength reduces), the water droplet is experience jetting at higher powers, which is not ideal for removing the ash for cleaning.

Figure 7(h) shows the estimated cleaning efficiency (defined by the cleaned area of a layer of dust due to the water droplet movements versus power for a 2  $\mu\text{L}$  of a water droplet). With a SAW power value between 1.82 W to 3.99 W, the cleaning efficiency is much better than that at powers less than 1.82 W and larger than 3.99 W. At lower powers, the water droplet is not able to remove some dusts easily due to the low pumping speed. Whereas at higher powers, the water droplet is experiencing jetting where dust would not be removed due to the very short interaction time between the dust particles and the fluid. Figure S2 in the supporting information summarises the moving speeds of the droplet versus the applied power for cleaning work. It corresponds to how fast it took the water droplet to drive away from the ash particles. Figure S3 in the supporting information summarizes the cleaning results based on the time taken for the water droplet to fully drive away the ash particles against the power applied, and it is complementing the droplet movements illustrated from Figure 7(a) to 7(f). As the power applied is increased, the droplet is transported much faster. The time taken for the water droplet to fully drive away the ash particles decrease as the SAW devices' wavelength decreases. In other words, as the frequency increases, the time required to drive away ash particles reduces as the power applied increases. However, based on Figures S3d to S3f in the supporting information, for the 155 MHz sample, at a power of 4.95 W, the water droplet is not efficient

enough to drive away the ash particles. The reason is at such a high frequency, the waves are significantly dampened, and the energy is being dissipated relatively faster into the water droplet.

Figure 8 shows the cleaning stages of starch powders and solutions which were deposited on the surface of the SAW device using the continuously supplied water droplet of 2  $\mu$ L. Figure 8 (a) to (d) are those results for dried solid starch powders. As the SAW power is applied, the water droplet has been pushed to move to the starch position as shown in Figure 8(b). Under the agitation of SAW power, the starch is quickly mixed with the water droplet, causing significant streaming inside the water droplet. During this process, more water droplets were continuously dispensed to effectively mix and drive the semi-solid starch particles as seen in Figure 8(c). Simultaneously the acoustic heating effect occurs, providing an effective role to dislodge particles from the surface by overcoming the adhesion forces of the liquid starch solution. Finally, the large water droplet was observed to be driven away as shown in Figure 8(d). Results clearly showed that with a combination of internal streaming and acoustic heating effects, the contaminated starch particles can be effectively driven away using the SAW device. Active surface cleaning was further demonstrated using a semi-liquid starch/water solution, which was dropped onto the SAW propagating paths, to simulate contaminants such as birds' excrement. Figure 8(e) to 8(h) shows the sequence of cleaning stages of liquid starch solution on the SAW device. Under the significantly internal streaming and acoustic heating effects, the liquid starch solution is observed to be fully driven away.

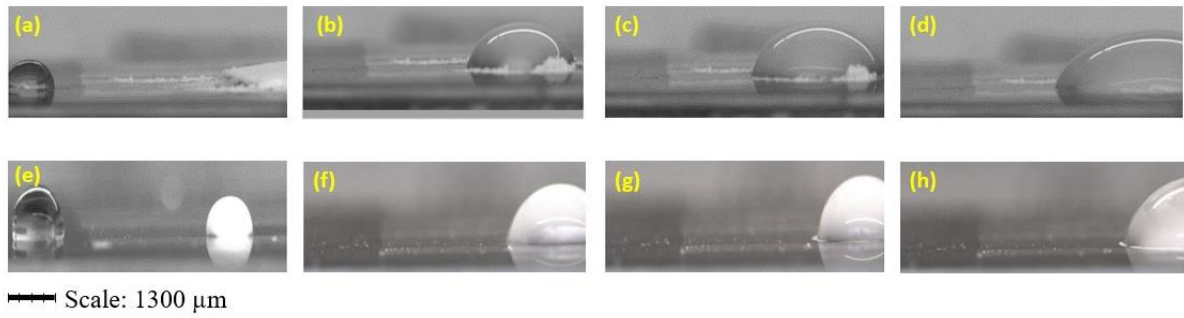


Figure 8 (Top line): Droplet transportation images with continuous dispensing of 2  $\mu\text{L}$  of water droplet to effectively drive solid particles away at: (a) 0 s, (b) 18.685 s, (c) 44.890 s, (d) 70.867 s ; (Bottom line) Droplet transportation images for starch mixture with continuous dispensing of 2  $\mu\text{L}$  water droplet at: (e) 0 s; (f) 1.936 s; (g) 10.705 s; (h) 38.492 s

### ***Thermal effects during acoustofluidics and cleaning***

Figure 7a shows acousto-thermal effects on the surface of the ZnO/glass SAW devices with a wavelength of 100  $\mu\text{m}$  at different applied powers. The surface temperature increases rapidly for 30 s during the heating process. Subsequently, a slow increase of the temperature can be observed from 30 s to 60 s. The maximum value of temperature is changed from 43°C to 98 °C with the applied power varied from 1.41 W to 7.59 W. The inset of Figure 7a shows the snapshot of an infrared image of the thermal distribution on the surface of the ZnO/glass SAW device using an applied power of 2.35 W. The heating rate of the thermal effect in the ZnO/glass device was determined by a linear fit of the highest temperature as a function of the applied power. The obtained results are shown in Figure 7b. The heating rates are obtained as 7.69 °C/W, 9.72 °C/W, 66.33°C/W and 30.73°C/W, corresponding to the thermal effects occurred on the ZnO/glass devices with the wavelengths of 100  $\mu\text{m}$ , 64  $\mu\text{m}$ , 32  $\mu\text{m}$  and 16  $\mu\text{m}$ , respectively. Comparing the above heating rates of the ZnO/glass devices with the values of 0.67~1.26 °C/W



measured in ZnO/ultra-nanocrystalline diamond (UNCD) SAW devices [17], it indicates that the low thermal conductivity of the glass substrate ( $1.5 \text{ W/m}\cdot\text{K}$ ) favors the improvement of heating rates at the MHz range, where the thermal conductivity of UNCD device is  $26 \text{ W/m}\cdot\text{K}$  [17, 40].

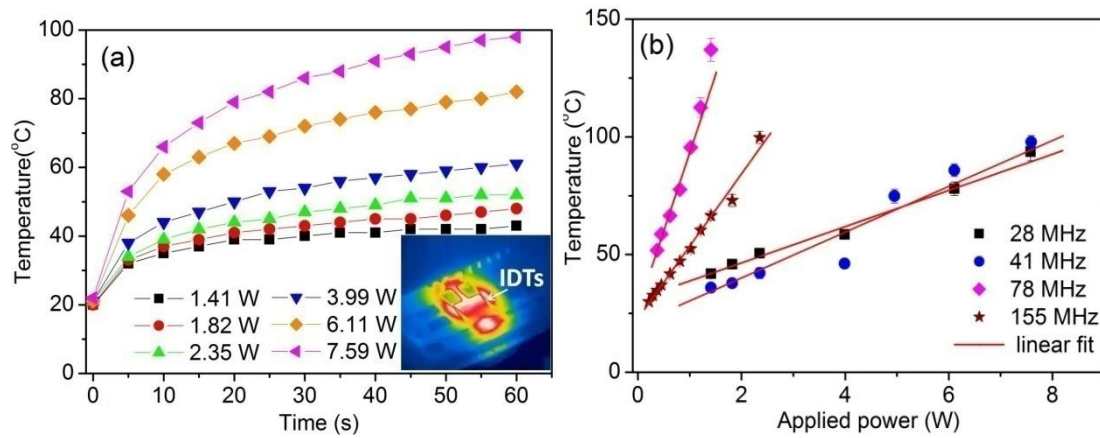


Figure 7 (a) the surface temperature of the ZnO/glass SAW device with a wavelength of  $100 \mu\text{m}$  as a function of the time using different applied powers, the inset shows the snapshot of infrared imaging of the thermal distribution on the surface of the ZnO/glass SAW device using an applied power of  $2.35 \text{ W}$ ; (b) the acoustic thermal effects between the temperature and the applied power for the Rayleigh waves excited using different resonant frequencies.

For active cleaning, the heating effect is a crucial factor. When the temperature increases, the SAW devices will be heated up, which can trigger the water droplet to effectively interact with surface contaminants and the surface contaminants can be more efficiently driven away during liquid transportation. In addition, based on the above results of acoustic heating, the ZnO/glass devices need to be monitored, and should be operated in the appropriate range of the applied power, which can be used to prevent overheating of samples and damaging the SAW electrodes

(IDTs).

#### **4. Conclusions**

In this paper, ZnO/glass SAW devices were fabricated and characterized. The acoustofluidics performance of these ZnO/Glass SAW devices were demonstrated where both pumping and jetting phenomenon were observed when the surface was treated with a hydrophobic layer. Nebulization of the water droplet on the nontreated sample surface was also demonstrated using the same devices. The transparent glass structures with integrated SAW devices are introduced as an active cleaning platform with contamination detection capability. Detection of dust formation is possible using the SAW devices as sensors based on the mass loading effect. Detection of contaminants and their subsequent removal were demonstrated in this paper. Surface cleaning of ash, starch particles and solutions, used as model contaminants, was demonstrated for different RF powers to evaluate the cleaning efficiency and thermal effect on ZnO/glass SAW devices. This active sensing and cleaning work can be further used for autonomous cleaning in the future by implementing a closed loop feedback.

#### **Declaration of Competing Interest**

The authors declare that they have no known competing financial interests.

#### **Acknowledgements**

This work was financially supported by the UK Engineering and Physical Sciences Research Council (EPSRC) under grant EP/P018998/1, Newton Mobility Grant (IE161019) through

Royal Society, the National Natural Science Foundation of China (11504291,52075162, 12104320), Research Project in Fundamental and Application Fields of Guangdong Province (2020A1515110561), Shenzhen Science & Technology Project (RCBS20200714114918249), the Innovation Leading Program of New and High-tech Industry of Hunan Province (2020GK2015), the Natural Science Foundation of Hunan Province (2021JJ20018), and the Natural Science Foundation of Changsha (kq2007026).

## **Appendix A. Supplementary material**

## **References**

- [1] B. Ziaie, A. Baldi, M. Lei, Y. Gu, R. A. Siegel, *Advanced Drug Delivery Reviews* 56(2), (2004) 145–172
- [2] Hou, X., Zhang, Y., Santiago, Gd. *et al.* Interplay between materials and microfluidics. *Nat Rev Mater* 2, 17016 (2017).
- [3] S. Neethirajan, I. Kobayashi, M. Nakajima, D. Wu, S. Nandagopal, F. Lin, *Lab Chip*, 11(9) (2011) 1574-1586
- [4] W. Connacher, N. Zhang, A. Huang, J. Mei, S. Zhang, T. Gopesh, J. Friend, *Lab Chip*, 18(14) (2018) 1952-1996
- [5] L. Y. Yeo, J. R. Friend, *Annu. Rev. Fluid Mech.*, 46 (2014) 379-406
- [6] M. Gedge and M. Hill, *Lab Chip*, 12 (2012) 2998–3007
- [7] Jiang, D., Liu, J., Pan, Y., Zhuang, L., Wang P., *Cell Tissue Res* 386(2), (2021) 215–226
- [8] Y.Q. Fu, J.K. Luo, N.T. Nguyen, A.J. Walton, A.J. Flewitt, X.T Zu, Y. Li, G. McHale, A.

Matthews. E. Iborra H. Du, W.I.Milne, Progress in Mater Sci.89 (2017), 31-91.

[9] J. Zhou, D. B. Xiao, Z. X. Song, M. Zhuo and X. Z. Wu, IEEE Micro Electro Mechanical Systems(MEMS)(2018) 79-82

[10]J. Zhou, X. L. He, W. B. Wang, Q. Zhu, W. P. Xuan, H. Jin, S. R. Dong, M. D. Wang, J. K. Luo, IEEE Electron Device Letters 34, (2013) 1319-1321

[11] J. H. Lim, C. K. Kong, K. K. Kim, I. K. Park, D. K. Hwang, and S. J. Park, Adv. Mater. 18(20), (2006) 2720-2724

[12] J. Zhou, X.Z.Wu, D.B. Xiao, M. Zhuo, H. Jin, J.K. Luo, Y.Q. Fu, Surface & Coatings Technology 320 (2017) 39-46

[13]W. B. Wang, H. Gu, X. L. He, W. P. Xuan, J. K. Chen, X. Z. Wang, J.K. Luo, Chinese Physics B 24(5), (2015) 057701

[14]X. L.He, J. Zhou, W. B. Wang, W. P. Xuan, D. J. Li, S. R. Dong, H. Jin, Y. Xu, J. K. Luo, Behav. Brain Sci, 1659 (2), (2014), 75-80

[15] K. H. Bang, D. K. Hwang, M. C. Jeong, K. S. Sohn, and J. M. Myoung,Solid State Commun., 126 (11), (2003) 623-627

[16] Y. N. Chanchangi, A. Ghosh, S. Sundaram, and T. K. Mallick, Renew. Sustain. Energy Rev., 121 (2020) 109704

[17] H. F. Pang, L. Garcia-Gancedo, Y.Q. Fu, S. Porro, Y.W. Gu, J. K. Luo, X. T. Zu, F. Placido, J.I.B. Wilson, A.J. Flewitt, W.I. Milne,Physica Status Solidi (a),210(8), (2013) 1575-1583

[18]M. Koyano, P. Quocbao, L. T. Thanhbinh, L. Hongha, N. Ngoclong, S. Katayama, Physica Status Solidi(a)193, (2002) 125-131

[19]Pang, H., Zhang, G., Tang, Y., Fu, Y., Wang, L., Zu, X., & Placido, F. Applied Surface

Science, 259 (2012) 747-753.

[20] Shih, W., Wang, T., & Pen, Y. Applied Surface Science, 258(14) (2012) 5424-5428.

[21] J.H. Wu, C. S. Yin, J. Zhou, H. L. Li, Y. Liu, Y. P. Shen, S. Garner, Y. Q. Fu, H. G. Duan, ACS Applied Materials & Interfaces 12 (35), (2020) 39817-39825

[22] M. Kadota, T. Kitamura, IEEE Trans. Ultrason., Ferroelectr. Freq. Control 46(4), (1999) 817-822

[23] M. Kadota, C. Kondoh, IEEE Trans. Ultrason., Ferroelectr. Freq. Control 44(3), (1997) 658-665

[24] Chen, Y., Hsu, J., & Wu, T. Journal Of The Chinese Institute Of Engineers, 27(6) (2004) 823-833.

[25] C. Caliendo, F. Laidoudi, Sensors, 20(5)(2020) 1380.

[26] J. Shen, S. Fu, R. Su, H. Xu, F. Zeng, C. Song, & F. Pan, Electronics, 10(1) (2020) 23.

[27] R. Tao, S. A. Hasan, H. Z. Wang, J. Zhou, J. T. Luo, G. McHale, D. Gibson, P. Canyelles-Pericas, M. D. Cooke, D. Wood, Y. Liu, Q. Wu, W. P. Ng, T. Franke, Y. Q. Fu, Scientific Report 8, (2018) 9052

[28] H. Zhang, H. Wang, Micromachines 12(11), (2021) 1286.

[29] Liu, Yong, Luo, Jing Ting, Zhao, Chao, Zhou, Jian, Hassan, Sameer, Li, Yifan, Cooke, Michael, Wu, Qiang, Ng, Wai Pang, Du, Jiang Feng, Liu, Yang and Fu, Yong Qing, IEEE Transactions on Electron Devices, 63 (11), (2016) 4535-4541

[30] Y. Wang, Q. Zhang, R. Tao, J. Xie, P. Canyelles-Pericas, H. Torun, J. Reboud, G. Mchale, L. E. Dodd, X. Yang, J. T. Luo, Q. Wu, Y. Q. Fu, ACS Appl. Mater. Interfaces, 13(14), (2021), 16978–16986

- [31]Y. Q. Fu, L. Garcia-Gancedo, H. F. Pang, S. Porro, Y. W. Gu, J. K. Luo, X. T. Zu, F. Placido, J. I. B. Wilson, A. J. Flewitt, W. I. Milne, *Biomicrofluidics*, 6(2), (2012) 024105
- [32]J. Li, M. H. Biroun, R. Tao, Y. Wang, H. Torun, N. Xu, M. Rahmati, Y. F. Li, D. Gibson, C. Fu, J. T. Luo, L. X. Dong, J. Xie, Y. Q. Fu, *J. Phys. D. Appl. Phys.*, 53(35), (2020) 355402
- [33]Y. J. Guo, A. Dennison, Y. F. Li, L. K. Luo, X. T. Zu, L. Mackay, P. Langridge-Smith, A. Walton, Y. Q. Fu, *Microfluid. Nanofluidics*, 19 (2), (2015) 273–282
- [34] Z. Chen, J. Zhou, H. Tang, Y. Liu, Y. Shen, X. Yin, J. Zheng, H. Zhang, J. Wu, X. Shi, Y. Chen, Y. Fu, H. Duan, *ACS Sensors* 5(6), (2020) 1657-1664
- [35] H. Wohltjen, *Sens. Actuators B* 5 (1984) 307-325
- [36]G. Potter, N. Tokranova, A. Rastegar, J. Castracane, *Microelectronic Engineering* 162, (2016) 100-104
- [37]H. Song, J. Lee, K. Y. Lee, and S. K. Chung, *Proc. IEEE Int. Conf. Micro Electro Mech. Syst.*, vol. 2020-January, (2020) 521–522,
- [38] H. Song, D. Jang, J. Lee, K. Yong Lee, and S. Kug Chung, *J. Micromechanics Microengineering*, 31(12) (2021) 125007
- [39]R. J. Shilton et al., “Rapid and controllable digital microfluidic heating by surface acoustic waves,” *Adv. Funct. Mater.*, vol. 25, no. 37, pp. 5895–5901, Oct. 2015, doi: 10.1002/ADFM.201501130.
- [40]Syed Ahmed, Romy Liske, Thomas Wunderer, Michael Leonhardt, Ronny Ziervogel, Charlee Fansler, Tim Grotjohn, Jes Asmussen, Thomas Schuelke, *Diamond & Related Materials* 15 (2006) 389 – 393.